Highlighting a study of polymer coating on NCM cathode active material particles from the group of Dr Felix H. Richter, Center for Materials Research, Institute of Physical Chemistry, Justus-Liebig-University Giessen, Germany.

Lithiated polymer coating for interface stabilization in Li_6PS_5Cl-based solid-state batteries with high-nickel NCM

This study demonstrates a scalable spray-coating method to apply a 1–3 nm sulfonated polyphenylene sulfone/ polyvinylpyrrolidone coating on NCM, enhancing interface stability and mitigating degradation in sulfide-based solid-state batteries.

As featured in:

See Felix H. Richter *et al.*,
J. Mater. Chem. A, 2025, **13**, 2600.

ROYAL SOCIETY
OF CHEMISTRY

rsc.li/materials-a

PAPER

Lithiated polymer coating for interface stabilization in Li$_6$PS$_5$Cl-based solid-state batteries with high-nickel NCM†

Bing-Xuan Shi,[a] Franjo Weber,[b] Yuriy Yusim,[a] Thomas Demuth,[c] Kilian Vettori,[a] Andreas Münchinger,[d] Giorgi Titvinidze, [de] Kerstin Volz,[c] Anja Henss,[a] Rüdiger Berger [b] and Felix H. Richter [*a]

Li$_6$PS$_5$Cl-based solid-state batteries with high-nickel LiNi$_{0.9}$Mn$_{0.05}$Co$_{0.05}$O$_2$ (NCM) promise higher energy density and safety than lithium-ion batteries with liquid electrolyte. However, their cycling performance is often limited by interface degradation between NCM and solid electrolyte. Here, a sulfonated polyphenylene sulfone/polyvinylpyrrolidone (sPPSLi/PVP) coating on NCM particles is presented that mitigates this issue. This uniform coating impedes direct contact between NCM and solid electrolyte, which lessens interface degradation and improves cycling performance. Electrochemical impedance spectroscopy and chronoamperometry show a reduced interface resistance and Li$^+$-ion transport length during cycling for sPPSLi/PVP-coated NCM in Li$_6$PS$_5$Cl-based solid-state batteries. Additionally, the coating effectively suppresses side reactions, particularly the formation of oxygenated species, at the NCM/SE interface. Overall, sPPSLi/PVP-coated NCM shows remarkable improvements in cycling stability and rate capability, emphasizing the significance of applying polymer coatings.

1. Introduction

An important sub-group of solid-state batteries is solid electrolyte batteries (SEBs) in which ion transport occurs through ion hopping in inorganic solid electrolytes (SEs), as classified by Sen and Richter.[1] They are promising alternatives to lithium-ion batteries, also called liquid electrolyte batteries (LEBs), as they promise to reach higher energy density[2,3] and enhanced safety.[4] The sulfide-based SE Li$_6$PS$_5$Cl exhibits sufficient ionic conductivity of around 2 mS cm^{-1} (ref. 5 and 6) for investigating the fundamental working principles of SEBs. Developing SEBs faces technical challenges,[7] particularly high interfacial resistance and instability between electrode materials and SEs.[8,9] Additionally, moisture sensitivity, densification, and the preparation of thin SE membranes complicate the fabrication of SEBs.[2,10]

In the SEB cathode, high-nickel LiNi$_{0.9}$Mn$_{0.05}$Co$_{0.05}$O$_2$ (NCM) as the cathode active material is advantageous in providing high energy density and low cost.[11,12] However, NCM suffers from poor cycling stability and surface instability when in contact with SEs.[13,14] Even at 0% state of charge (SOC), NCM and Li$_6$PS$_5$Cl chemically react at the interface, leading to capacity fading.[15] The cathodic instability of Li$_6$PS$_5$Cl leads to electrochemical degradation at the electrode–electrolyte interface, which decreases Coulomb efficiency.[16–19] In addition, oxidation reactions at the NCM/SE interface coupled with NCM oxygen loss occur at high SOC (around 3.5 vs. In/LiIn), forming a passivation layer with oxygenated species.[20–22] Chemomechanical fracture of NCM particles is also significantly driven by oxygen loss at the NCM/SE interface.[8,23,24]

Surface coatings on NCM are applied to alleviate the interface stability between NCM and Li$_6$PS$_5$Cl. Hence, they should be made of a material that is electronically insulating and electrochemically stable.[25] However, such a coating may restrict electronic conduction within the cathode, which needs to be taken into account. Regarding ionic conductivity of the coating, it is to be noted that to keep Li$^+$ transport resistance below 1 Ω cm^2 with a 1 nm thick coating, an ionic conductivity of only 10^{-4} mS cm^{-1} is sufficient.[26] Overall, this necessitates optimization of the coating thickness and coverage to avoid impeding electron and Li$^+$ transport between particles.

Many inorganic materials have been developed as surface coatings for NCM,[27] such as metal oxides, including LiNbO$_3$,[28–30] Li$_6$ZnNb$_4$O$_{14}$,[31] LiAlO$_2$,[32] Li$_2$ZrO$_3$,[29,33] Li$_4$Ti$_5$O$_{12}$,[34] Li$_3$BO$_3$,[35]

aInstitute of Physical Chemistry & Center for Materials Research (LaMa), Justus-Liebig-University Giessen, Heinrich-Buff-Ring 17, 35392 Giessen, Germany. E-mail: Felix.H.Richter@phys.chemie.uni-giessen.de

bMax Planck Institute for Polymer Research, Ackermannweg 10, 55128, Mainz, Germany

cDepartment of Physics & Materials Sciences Center (WZMW), Philipps-University Marburg, Hans-Meerwein Straße 6, 35032 Marburg, Germany

dHahn-Schickard, Georges-Köhler-Allee 103, 79110 Freiburg, Germany

eAgricultural University of Georgia, 240 David Aghmashenebeli Alley, 0131 Tbilisi, Georgia

$Li_2B_4O_7$,[36] and $Li_3B_{11}O_{18}$;[37] and halide electrolytes including Li_3YCl_6.[38] However, inorganic coatings can crack or detach during volume change of NCM.[26] Compared to the elastic modulus of ceramics like $LiNbO_3$ (∼195 GPa), polymers have a lower elastic modulus (∼6 GPa), which is close to that of thiophosphate-based SEs (∼20 GPa).[26,39] Polymers are also expected to bind more readily to NCM, reducing fractures at particle contact points.[26] However, it needs to be considered that the mechanical properties of nanometer-thick coatings may differ from bulk properties due to polymer chain rearrangement at the surface or interfacial interactions with NCM.[40,41]

Deng *et al.* explored modifying NCM and carbon additives with poly(3,4-ethylenedioxythiophene) (PEDOT) *via* molecular layer deposition in a $^{In}SEB^{NCM}$.[42] In addition, NCMs coated with polymers such as polyvinylpyrrolidone (PVP),[43] PEDOT,[44] poly(3,4-ethylene dioxythiophene)-*co*-poly(ethylene glycol) (PEDOT-*co*-PEG),[45,46] polyacrylonitrile,[47] polyaniline,[48] poly(t-ris(2-(acryloyloxy)ethyl) phosphate),[49] polysiloxane,[50] Nafion,[51] bis(carboxyethylgermanium)-based polymer,[52] and poly-pyrrole[53] have been tested in a variety of LEBs. Our previous work introduced a polycation coating of poly((4-vinyl benzyl) trimethylammonium bis(trifluoromethanesulfonylimide)) (PVBTATFSI), applied through a scalable spray drying method to improve the NCM/SE interface durability and $^{LiIn}SEB^{NCM}$ cycling performance.[54]

However, the lack of Li^+ in the PVBTATFSI coating may not be ideal, which is why we test sulfonated poly(phenylene sulfone) in its lithiated form (sPPSLi, Fig. S1†) in the study presented here. Sulfonated polyphenylene sulfone is a material known for its superior proton conductivity and low water transport rates, which is excellent for use as an electrolyte in polymer electrolyte membrane fuel cells.[55] It has a high glass transition temperature exceeding 300 °C at which polymer decomposition starts. Additionally, the aromatic backbone offers superior thermal and oxidative stability compared to other sulfonated poly(arylene) polymers, enhancing its suitability for environments that demand high durability and resistance to degradation.[55,56] Therefore, sPPSLi is expected to be an excellent candidate for polymer coatings in SEBs. This is because maintaining a high glass transition temperature ensures that sPPSLi retains its mechanical strength and stability both during the coating process and throughout the operation of the device.

Here, we present polymer coatings that reduce NCM surface degradation and enhance the electrochemical performance of SEBs. A blend of sPPSLi and PVP is coated on $LiNi_{0.9}Mn_{0.05}Co_{0.05}O_2$ particles by spray drying, which reduces capacity loss at the NCM/SE interface. The addition of PVP is required to create a strong bond between NCM and sPPSLi, which enhances interface stability.[43] Analysis of interfacial degradation and Li^+ pathways demonstrate improved electrochemical cycling of a Li_6PS_5Cl-based $^{LiIn}SEB^{NCM}$ with sPPSLi/PVP-coated NCM.

2. Results and discussion

2.1 Characterization of sPPSLi/PVP-coated NCM

We first attempted to apply a 1 wt% anionic sPPSLi coating on NCM (without PVP) using a spray drying apparatus. During spray-drying, the precursor solution is atomized into fine ≈25 μm droplets and quickly dried to coat the NCM surface, ensuring the final composition matches the precursor solution. For reasons of consistency and comparability, the nominal content of 1 wt% of polymer is based on our previous findings that produced a 2 nm coating thickness with cationic PVBTATFSI of the same nominal content.[54] If required, the weight ratio can be further optimized in future work. Unfortunately, water and alcohols that are often good solvents for anionic polymers can leach Li^+ from NCM when exposed to protic solvents during the coating process. To avoid this issue, sPPSLi is dissolved in dimethylformamide (DMF) for the coating of NCM by spray drying.[57] Scanning electron microscopy (SEM) images of the produced sPPSLi-NCM samples show localized deposition of particulate sPPSLi polymer on the sPPSLi-NCM surface (Fig. S2†). The results indicate that the electrostatic attraction between sPPSLi and NCM is insufficient to form a uniform coating on its own. This may be due to layered oxides displaying a negative zeta potential, favoring electrostatic attraction to polycations rather than polyanions in neutral to basic conditions.[58]

Consequently, we use PVP as a coating mediator for sPPSLi, which facilitates a uniform coating of both polymers on NCM.[43] A 1 : 1 weight ratio of PVP to sPPSLi (1 wt% of coating in total compared to NCM) is chosen here to demonstrate its feasibility. SEM images of the produced sPPSLi/PVP-NCM coated powder demonstrate a marked reduction in isolated polymer particles, as shown in Fig. S2.† It is worth noting that a stable and transparent polymer true solution (solute particle size less than 1 nm) is necessary for the spray drying process to form a uniform coating. sPPSLi and PVP create a transparent and stable solution in DMF, which is different to some other polymers that precipitate when mixing with PVP.[59] Using infrared spectroscopy, we find that PVP manifests a robust electrostatic attraction with sPPSLi, indicated by the red-shift in C=O stretching mode from 1669 cm^{-1} to 1656 cm^{-1}, as shown in Fig. S3.† Together, these results suggest a uniform and homogeneous sPPSLi/PVP coating is present on sPPSLi/PVP-NCM as there is no apparent difference in SEM images between pristine NCM (pNCM) and sPPSLi/PVP-NCM.

We use transmission electron microscopy (TEM) to compare pNCM and sPPSLi/PVP-NCM samples. The TEM images in Fig. 1 show that pNCM does not have a surface coating and that sPPSLi/PVP-NCM has an amorphous coating of around 1–3 nm thickness, as is evident from the amorphous surface layer that lies on top of the lattice planes of NCM. Although every investigated particle exhibits a uniform coating layer, TEM alone cannot confirm the chemical composition of the coating. Therefore, we use scanning force microscopy based infrared microscopy (nano-IR) in photo-induced force microscopy mode to verify the composition and distribution of the sPPSLi/PVP coating on the NCM substrate.

In nano-IR (Fig. S4†), an IR laser is focused on the tip of a scanning force microscope. For samples that interact with IR light of a specific wavenumber, photo-induced forces are generated. The photo-induced forces excite oscillation of the cantilever, which can be detected by the photodiode *via* the

This journal is © The Royal Society of Chemistry 2025

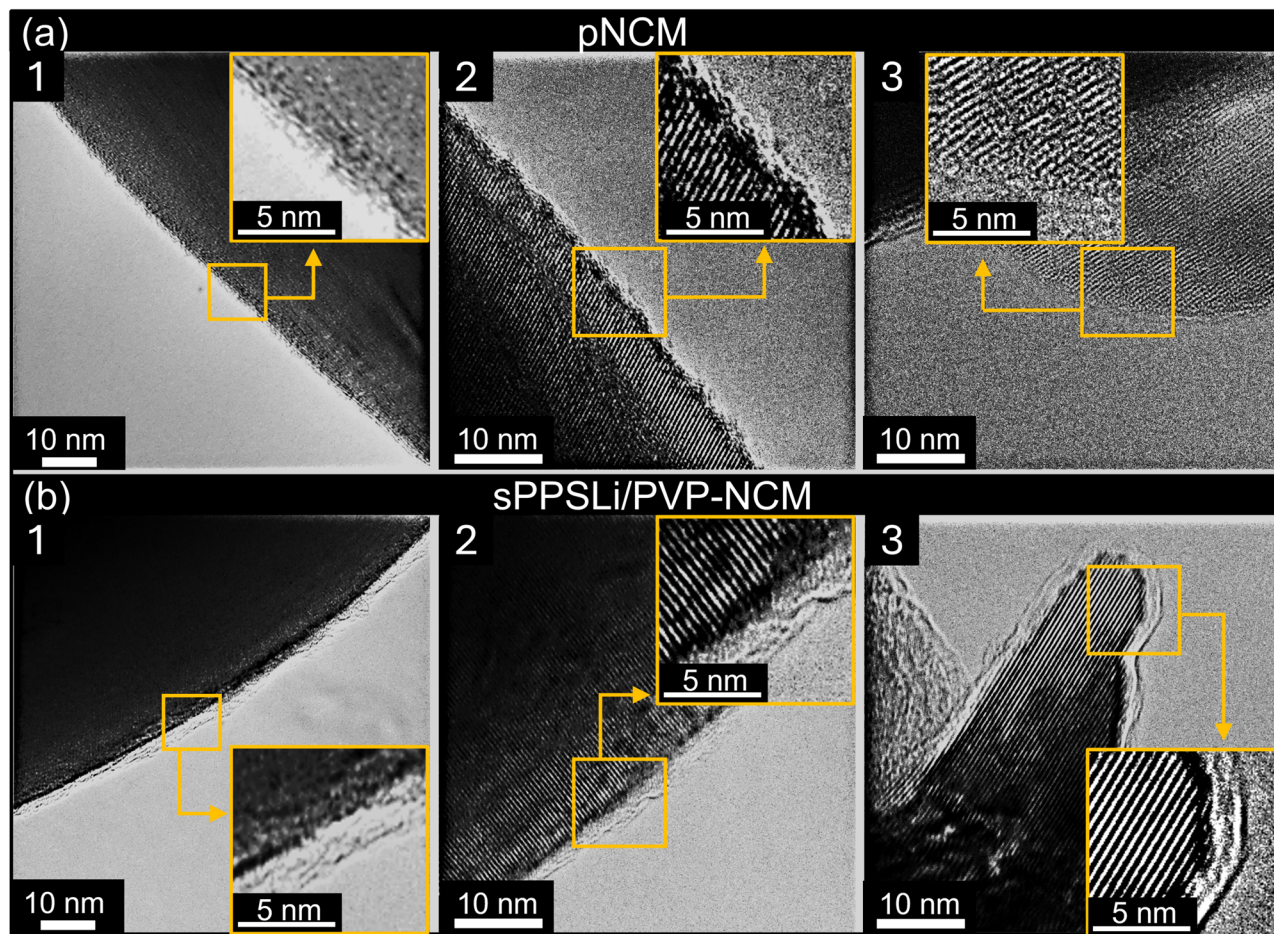*J. Mater. Chem. A*, 2025, **13**, 2600–2614 | **2601**

Fig. 1 TEM images of (a) pNCM and (b) sPPSLi/PVP-NCM. The insets show a magnification of the coating layer, providing a clearer presentation of its thickness of around 1 to 3 nm. Each panel is labeled from 1 to 3, showing different particles.

deflected laser beam.[60] The amplitude of oscillation is directly correlated to the absorption of the sample at the used IR wavenumber.[61] For polymer samples, this method has proven useful for determining their lateral distribution.[62]

To verify the polymer on top of the NCM particles, we record nano-IR spectra at several locations on a coated NCM particle (Fig. 2a) and on a reference sample of the polymer (Fig. S5†). Both spectra show the same carbonyl stretching mode and fingerprint between 1500 cm^{-1} and 1000 cm^{-1} (Fig. 2b). The carbonyl stretching shift in the sPPSLi/PVP-NCM nano-IR spectrum, compared to sPPSLi/PVP, likely arises from the unique mechanical properties of nanometer-thick coatings, influenced by polymer chain rearrangement and interactions with NCM.[40,41]

The nano-IR spectra are also identical to the far field Fourier transform infrared spectroscopy (FTIR) absorption spectrum of the polymer. The equivalence of the spectra confirms that the NCM particles are coated with a blend of sPPSLi and PVP. To find potential pinholes in the polymer coating, we scan the surfaces while detecting the nano-IR response at 1677 cm^{-1}, which corresponds to the stretching mode of the carbonyl double bond (Fig. 2c). The nano-IR signal never vanishes in this measurement. We conclude that the sPPSLi/PVP coating is

present at every tip position and that the NCM particles are practically fully covered with a layer of sPPSLi/PVP.

To chemically identify the sPPSLi/PVP coating on NCM, time of flight secondary ion mass spectrometry (ToF-SIMS) is used as surface sensitive technique. Therefore, mass spectra of the reference materials such as sPPSLi, PVP and NCM are compared to mass spectra of sPPSLi/PVP-NCM. As illustrated in Fig. 2d, the reference signals for SO^-, C_2SO^- (representing sPPSLi) and $C_3H_6NO^-$ (representing PVP) can be identified on the surface of sPPSLi/PVP-NCM, which confirms the presence of the coating. The NiO_2^- fragment (representing NCM) is also detected, which is probably due to the partial removal of the polymer coating under Bi^{3+} primary ions in the imaging mode.[63] When analyzing the surface in the imaging mode with Bi^{3+} as primary ions (0.1 pA), it can be seen that the intensity of the coating fragments decreases and the intensity of the NCM fragments increases with increasing ion dose (Fig. S6†). This indicates that the polymer coating is gradually removed during the measurement, confirming its very thin nature.

Based on the SEM, TEM, nano-IR, and ToF-SIMS analyses, the sPPSLi/PVP-NCM particles exhibit a uniform 1–3 nm thick coating layer of sPPSLi/PVP. This indicates that the sPPSLi/PVP coating may prevent direct physical contact between NCM and

2602 | J. Mater. Chem. A, 2025, **13**, 2600–2614

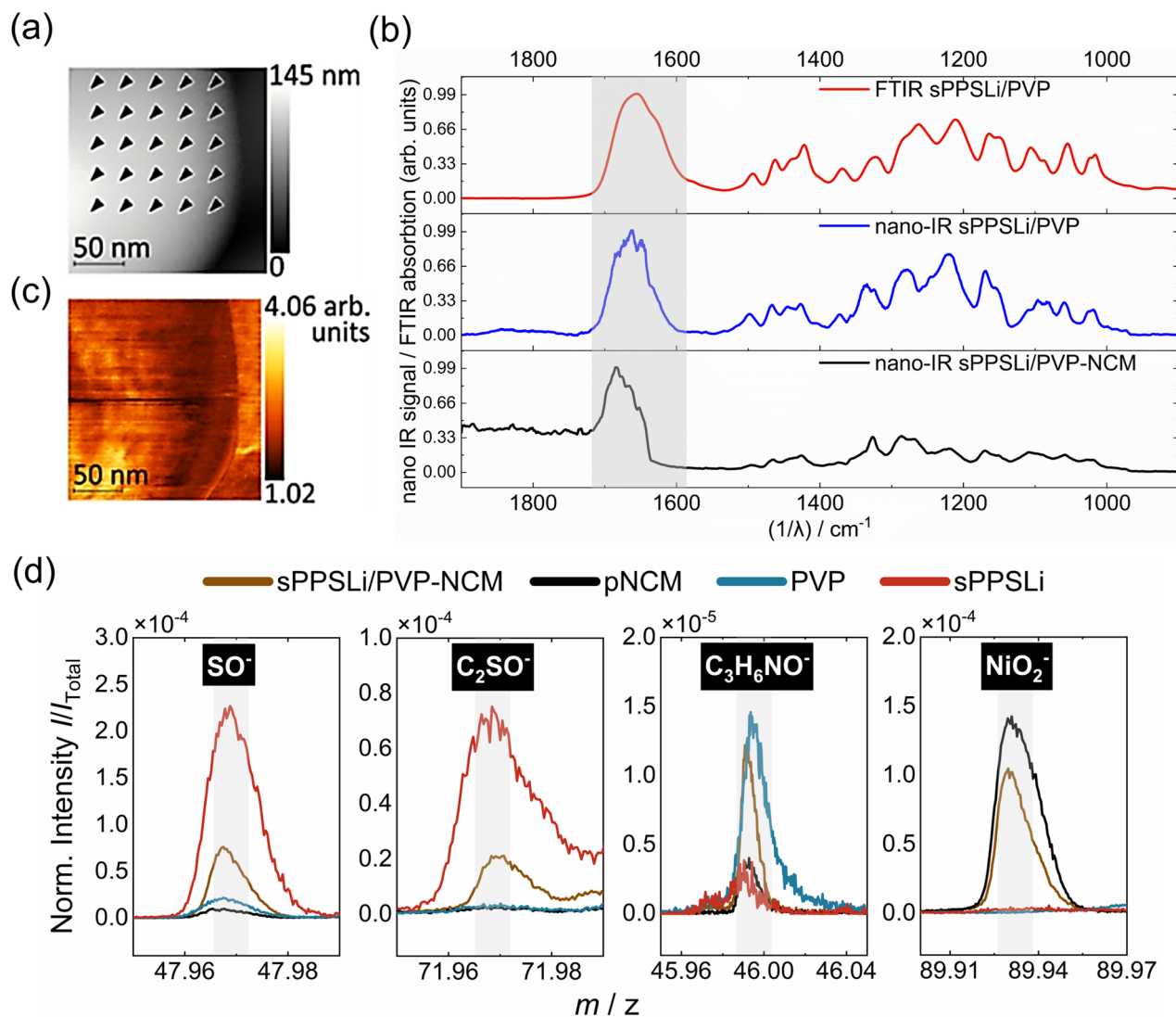This journal is © The Royal Society of Chemistry 2025

Fig. 2 (a) The topography of a sPPSLi/PVP-NCM particle with positions indicated as triangles where nano-IR spectroscopy is performed. (b) Fourier-transform infrared (FTIR) spectrum of sPPSLi/PVP polymer reference, nano-IR spectrum of sPPSLi/PVP polymer reference, and nano-IR spectrum of sPPSLi/PVP-NCM particles. (c) The stretching mode of the carbonyl double bond (1677 cm^{-1}) is adopted for nano-IR mapping at the same particle as shown in (a). (d) ToF-SIMS analysis of sPPSLi/PVP-NCM, pNCM, PVP and sPPSLi.

SE. The thickness of the sPPSLi/PVP coating of 1–3 nm matches the coating thickness observed to be suitable for coatings of poly(3,4-ethylene dioxythiophene)[42] and cationic polymer PVBTATFSI as well.[54]

2.2 Chemical and electrochemical stability between sPPSLi/PVP and Li$_6$PS$_5$Cl

The chemical stability of sPPSLi/PVP and Li$_6$PS$_5$Cl is investigated by X-ray diffraction (XRD) and FTIR analyses. Prior to XRD and FTIR analysis, a mixture of sPPSLi/PVP polymer and Li$_6$PS$_5$Cl is heated in a vacuum chamber at 80 °C for 24 hours to test whether there is a chemical reaction between the two compounds. The FTIR spectra of the mixed composite before and after heating are identical (Fig. S7a†). This suggests that the molecular structure of the polymer remains unchanged during the heating process. Moreover, the XRD result shows that the

mixed composite of the sPPSLi/PVP polymer and Li$_6$PS$_5$Cl after 80 °C heating is identical to pristine Li$_6$PS$_5$Cl without any heat treatment, which indicates that the bulk structure of Li$_6$PS$_5$Cl of the mixed composite is not altered (see Fig. S7b†). Overall, the FTIR and XRD measurements indicate that sPPSLi/PVP polymer is chemically stable to Li$_6$PS$_5$Cl.

To assess the electrochemical stability of the sPPSLi/PVP polymer with Li$_6$PS$_5$Cl, vapor-grown carbon fibers (VGCFs) are coated with the sPPSLi/PVP polymer utilizing the same spray drying method. Polymer-coated or pristine VGCF is used as the working electrode in combination with a LiIn alloy counter electrode to compare potential side reactions. 80 mg of Li$_6$PS$_5$Cl is adopted as the separator. Subsequently, the electrochemical stability of the sPPSLi/PVP polymer with Li$_6$PS$_5$Cl is evaluated through cyclic voltammetry, with scanning range from 0 V to 4.5 V (vs. In/LiIn). As evident in Fig. S8,† the sPPSLi/PVP-coated

This journal is © The Royal Society of Chemistry 2025

J. Mater. Chem. A, 2025, 13, 2600–2614 | 2603

VGCF exhibits a diminished current density and has no additional side reaction peaks compared to pristine VGCF, indicating that the sPPSLi/PVP polymer coating is electrochemically stable to Li_6PS_5Cl.

2.3 Impact of coatings on rate capability

To assess how the presented coatings affect the rate capability of SEBs, pellet-type cells are prepared with Li_6PS_5Cl and cycled under C-rates of 0.1C, 0.25C, 0.5C, 1C (1C corresponds to 2.1 mA cm^{-2}). The general configuration of the $^{LiIn}SEB^{NCM}$ is LiIn|Li_6-PS_5Cl|Li_6PS_5Cl/VGCF/NCM, as shown in Fig. S9a.† The rate capability results with pNCM and sPPSLi/PVP-NCM are shown in Fig. 3. Additionally, 1 wt% PVP-coated NCM (PVP-NCM), and 1 wt% PVBTATFSI-coated NCM (PVBTATFSI-NCM) are prepared and tested here to investigate two polymer coatings that do not contain lithium. In comparison, the lithium-containing polymer coating sPPSLi/PVP-NCM demonstrates a considerable improvement in specific capacity (q), particularly at high C-rates.

In the first cycle, pNCM has 183 mA h g^{-1} discharge capacity and 77% Coulomb efficiency; PVBTATFSI-NCM has 170 mA h g^{-1} discharge capacity and 79% Coulomb efficiency; and sPPSLi/PVP-NCM has 188 mA h g^{-1} discharge capacity and 80% Coulomb efficiency. The first cycle Coulomb efficiency is affected by the limited reversibility of Li^+-insertion in the H1 phase of the NCM bulk material.[64] Another contributing factor may be fewer side reactions at the NCM/SE interface.[65] As the coating mainly alters surface rather than bulk properties, the improved discharge capacity and Coulomb efficiency for sPPSLi/PVP-NCM should be due to reduced side reactions and improved interfacial kinetics at the electrode–electrolyte interface.

In contrast, PVP-NCM only achieves 138 mA h g^{-1} discharge capacity and 70% Coulomb efficiency in the first cycle. Among the compared SEBs, the PVP-NCM displayed the lowest capacity across all C-rates. This may be attributed to the insulation of NCM particles through the PVP coating that might obstruct Li^+ and/or electron transport. As some capacity remains, not all NCM surfaces appear to be fully blocked, indicating partial coverage of the NCM with PVP. Partial PVP coverage can be explained by the cell preparation causing damage to the PVP layer and exposing NCM to the electrolyte. This example shows that not any polymer can simply be coated to automatically improve cycling performance, but that careful further analysis into the properties required of a suitable polymer coating must be done.
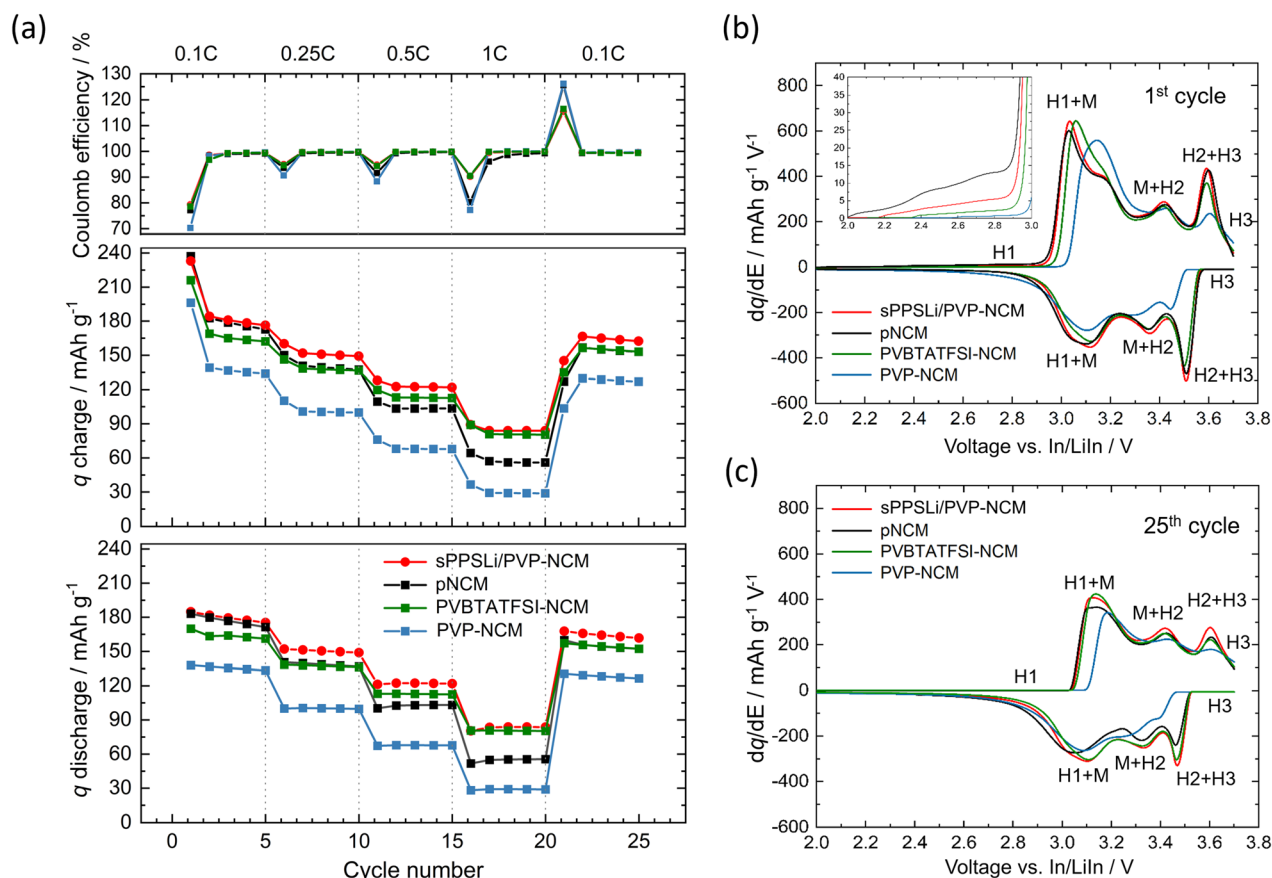

Fig. 3 (a) Specific capacity q and Coulomb efficiency at different C-rates of $^{LiIn}SEB^{NCM}$ using pNCM, sPPSLi/PVP-NCM, PVP–NCM, or PVBTATFSI–NCM, tested at C-rates of 0.1C to 1C in a pellet-type cell (LiIn|Li_6PS_5Cl|Li_6PS_5Cl/VGCF/NCM) with 2.1 mA h cm^{-2} nominal area capacity. Differential capacity dq/dE at 0.1C (b) in the 1st cycle and (c) in the 25th cycle. The inset in (b) shows an enlargement from 2–3 V (vs. In/LiIn) of the 1st cycle.

2604 | J. Mater. Chem. A, 2025, 13, 2600–2614

This journal is © The Royal Society of Chemistry 2025

Fig. 3b and c depict the Differential capacity dq/dE of the first and 25th cycle, respectively. Fig. S10† depicts the charge/discharge curves for the first and 25th cycle at a rate of 0.1C. In the first cycle, the differential capacity plots show similar areas above 3.48 V (*vs.* In/LiIn) for sPPSLi/PVP-NCM and pNCM during initial charging, suggesting that the sPPSLi/PVP coating does not affect the H2 + H3 phase transition.[23] Subsequently, sPPSLi/PVP-NCM shows clearer H2 + H3 phase transition than pNCM in the first discharge cycle. Additionally, the inset within Fig. 3b shows that all coated NCM have lower differential capacity than pNCM below 3 V (*vs.* In/LiIn) during initial charging, indicating less electrochemical degradation of Li$_6$-PS$_5$Cl for all coated NCM compared to pNCM.[66] The electrochemical degradation is indicative of the oxidation of Li$_6$PS$_5$Cl forming sulfur and P$_2$S$_5$ starting from about 2 V *vs.* In/LiIn.[17,19] H1/M (3 V *vs.* In/LiIn) and H2/H3 (3.6 V *vs.* In/LiIn) transitions are primarily influenced by active mass utilization and kinetic limitations at the NCM|Li$_6$PS$_5$Cl interface.[23] The first cycle dq/dE result reflects the improvement of the first cycle Coulomb efficiency.

At the 25th cycle, sPPSLi/PVP-NCM demonstrates improved reversibility and higher differential capacity compared to pNCM and other coated NCM above 3.48 V *vs.* In/LiIn. This process is associated with the H2 + H3 phase transition, as illustrated in Fig. 3c. The improved H2 + H3 phase transition indicates that the sPPSLi/PVP coating mitigates electrochemical degradation caused by oxidative reactions and chemo-mechanical degradation in this voltage range.[22,23,67] In conclusion, sPPSLi/PVP-NCM shows the best performance of all tested materials, which is mainly due to minimized side reactions without hindering the H2 + H3 phase transitions.

2.4 Evaluation of cycling performance and active mass

To assess the cycling performance, ^{LiIn}SEB$^{sPPSLi/PVP-NCM}$ and ^{LiIn}SEB^{pNCM} are investigated using the method as shown in Fig. S9b.†[54] First, the SEBs undergo 0.1C galvanostatic charging to 3.15 V (*vs.* In/LiIn). Then chronoamperometry is performed holding the potential at 3.15 V (*vs.* In/LiIn) until the current decreases to 2%. Chronoamperometry ensures that the impedance can be measured at a fixed SOC at 3.15 V (*vs.* In/LiIn). Following this, electrochemical impedance spectroscopy (EIS) is conducted at 3.15 V (*vs.* In/LiIn), ranging from 1 MHz to 100 μHz. As the charge transfer resistance (R_{ct}) varies with changes in the SOC, the chosen potential of 3.15 V (*vs.* In/LiIn) ensures high Li$^+$ diffusion coefficient and low R_{ct}.[68,69] Additionally, compared to 3.7 V (*vs.* In/LiIn) after the charging step, 3.15 V (*vs.* In/LiIn) prevents notable degradation during measurement. The SEBs are charged to 3.7 V (*vs.* In/LiIn) and then relaxed for 2 hours. They are then discharged to 2.0 V (*vs.* In/LiIn) with another 2 hours relaxation period. These relaxation periods determine the active mass, which refers to the quantity of NCM involved in the charging and discharging process.[23,54]

Fig. 4a compares the 0.1C cycling performance of sPPSLi/PVP-NCM and pNCM. Initially, the sPPSLi/PVP-NCM displays a discharge capacity of 186 mA h g^{-1}, higher than that of pNCM

(181 mA h g^{-1}). After 100 cycles, sPPSLi/PVP-NCM retains 78.3% of its capacity, whereas pNCM retains approximately 69%. After increasing the number of cycles to 152 at the same 0.1C rate, the sPPSLi/PVP-NCM retains a capacity of 71.6%, whereas pNCM has decreased to 59.6%. The larger capacity retention for sPPSLi/PVP-NCM demonstrates that the sPPSLi/PVP polymer coating enhances the long-term cycling stability in SEBs.

Fig. 4b demonstrates a comprehensive comparison of the active mass (m_{act}) calculation results of the tested SEBs. A cell consisting of NCM and a lithium–indium alloy anode has an open-circuit voltage (OCV) with a well-defined correlation to the SOC. The SOC represents the lithium content (denoted as '*x*' in Li$_x$Ni$_{0.9}$Mn$_{0.05}$Co$_{0.05}$O$_2$) within NCM. A LEB consisting of NCM and a lithium anode is used to obtain the reference correlation function of OCV *vs.* SOC (Fig. S11†). By utilizing a LEB for the reference correlation function, the influence of contact loss between NCM and the liquid electrolyte on the measurement can be minimized.[70] Based on reference data of the OCV *vs.* SOC, we can ascertain the specific discharge capacity at a particular SOC (q_{SOC}). Consequently, the m_{act} can be acquired using the measured discharge capacity (Q_{meas}) and q_{SOC} *via* eqn (1):[23,54]

$$m_{act}(g) = \frac{Q_{meas}\ (\text{mA h})}{q_{SOC}\left(\dfrac{\text{mA h}}{\text{g}}\right)} \tag{1}$$

sPPSLi/PVP-NCM displays an m_{act} retention of 83.7% after the 152nd cycle, which is higher than that of pNCM (78.8%). The loss of m_{act} is primarily attributed to contact loss, which isolates some NCM particles causing irreversible capacity decay. Contact loss is assumed to encompass two surface degradation mechanisms: firstly, the formation of an electrochemically inactive interfacial layer due to unwanted side reactions (including chemical, electrochemical, and chemo-mechanical degradations); and secondly, the physical separation between the NCM and Li$_6$PS$_5$Cl materials. These mechanisms reduce the effective contact area between NCM and Li$_6$PS$_5$Cl during cycling, resulting in active mass loss and elevated interface resistance. Therefore, both contact loss mechanisms have a comparable impact on battery performance, making their experimental differentiation difficult. Overall, the sPPSLi/PVP coating improves SEB performance by mitigating detrimental contact loss.

On the other hand, a passivation layer and particle cracking within NCM can extend the Li$^+$ diffusion pathway. Once cracks form within NCM particles, SEs cannot penetrate these cracks, which leads to an increase of the Li$^+$ diffusion pathway. The formation of cracks within NCM particles has a stronger influence on the Li$^+$ diffusion pathway than on the charge transfer at the interface.[23] This increased Li$^+$ diffusion pathway length causes the disparity between the measured specific discharge capacity (q_{meas}) and the specific capacity contributed by m_{act} (q_{act}) during cycling.[23] The q_{act} is obtained by m_{act} retention and the first cycle q_{meas} *via* eqn (2):[23]

$$\frac{n^{th}\text{cycle } m_{act}(g)}{1^{st}\text{cycle } m_{act}(g)} \times 1^{st}\text{cycle } q_{meas} = q_{act} \text{ at } n^{th}\text{cycle} \tag{2}$$

This journal is © The Royal Society of Chemistry 2025

J. Mater. Chem. A, 2025, **13**, 2600–2614 | **2605**
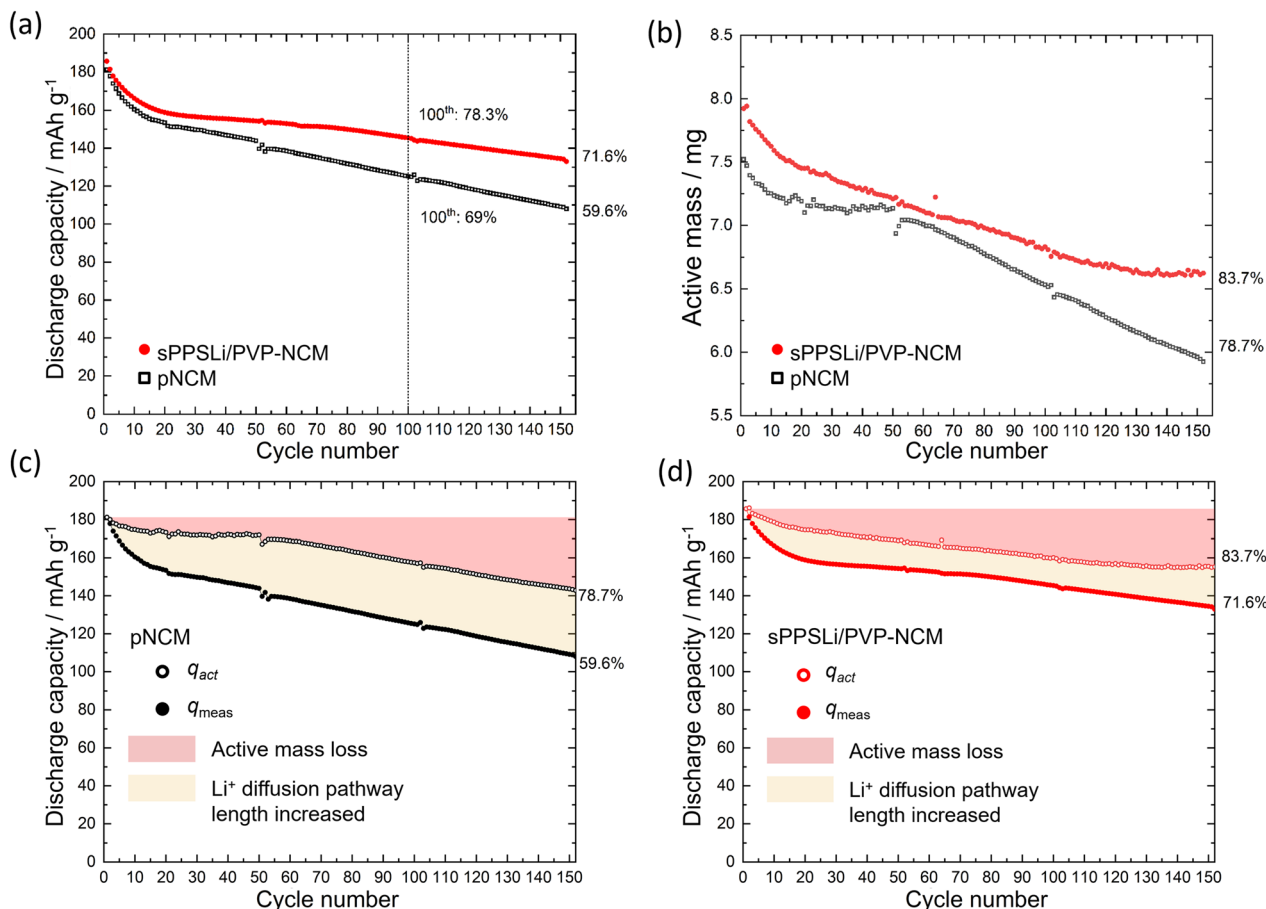
Fig. 4 (a) Cycling performance at 0.1C of $^{LiIn}SEB^{pNCM}$ and $^{LiIn}SEB^{sPPSLi/PVP-NCM}$ at 25 °C. (b) Corresponding evolution of m_{act}. For (c) pNCM and (d) sPPSLi/PVP-NCM, capacity loss is plotted, respectively, and split into the loss of m_{act} and the loss due to increased Li$^+$ diffusion pathway length. The pink area represents the loss of m_{act}. The yellow area illustrates the increasing Li$^+$ diffusion pathway length, determined as the difference between q_{meas} and q_{act}.

The q_{act} is compared with q_{meas}, as shown in Fig. 4c and d. The capacity decay caused by the increase of the Li$^+$ diffusion pathway length is assumed as the difference between q_{meas} and q_{act}. The $^{LiIn}SEB^{pNCM}$ exhibits a more pronounced increase in Li$^+$ diffusion pathway length and a more significant m_{act} loss (see Fig. 4c) than the $^{LiIn}SEB^{sPPSLi/PVP-NCM}$ (see Fig. 4d). In the following sections of this paper, we analyze how the sPPSLi/PVP coating mitigates both contact loss and increase of Li$^+$ diffusion pathway length.

2.5 Interfacial degradation analyzed by EIS and ToF-SIMS

To explore contact loss in-depth, the interfacial resistance in SEBs is measured at 3.15 V (vs. In/LiIn) under 0.1C by EIS, as mentioned in Section 2.4. The impedance data and fitting results using the transition line model[22,71] are shown in Fig. 5. The transition line model is used to characterize the resistance of the composite cathode, including electronic resistance (R_{ele}), ionic transport resistance (R_{ion}), and charge transfer resistance (R_{ct}), as shown in Fig. 5a. The finite-space Warburg element of cylindrical particles (Z_{fs}) describes the complex geometry of Li$^+$ diffusion in NCM by fitting the finite space diffusion tail in the Nyquist plot. C_{dc} stands for the differential capacitance of NCM. C_{int} and C_{ion}

denote the constant phase element related to the interfacial capacitance and ionic transport capacitance within the cathode composite, respectively. The transition line model coupled with electrolyte resistance (R_Ω), resistance of anode (R_{anode}), and anode capacitance (C_{anode}) are used to model the whole SEB.[22]

R_{ct} is employed as a metric for contact loss and interface degradation. However, it is challenging to extract R_{ct} from the EIS data using a transition line model. This is because the impedance follows a typical Gerischer-type relationship.[67] Consequently, we determine the composite resistance of the cathode, denoted as $R_{cathode}$. This is defined as the geometric mean of R_{ct} and the sum of R_{ele} and R_{ion} via eqn (3):

$$R_{cathode} = \sqrt{R_{ct} \times (R_{ele} + R_{ion})} \qquad (3)$$

The fitting results are shown in Fig. 5c and Table S1.† In the initial cycle at a voltage of 3.15 V (vs. In/LiIn), it is observed that $R_{cathode}$ of sPPSLi/PVP-NCM is 8 Ω cm^2 higher than that of pNCM (18 Ω cm^2 for pNCM and 26 Ω cm^2 for sPPSLi/PVP-NCM). The observed deviation may arise from the additional charge transfer and Li$^+$ transport resistances of the coating. It is worth noting that ionic conductivity of sPPSLi/PVP polymer is around 3.4×10^{-8} S cm^{-1} at 25 °C (Fig. S12†). This indicates that a ~1–

2606 | J. Mater. Chem. A, 2025, 13, 2600–2614

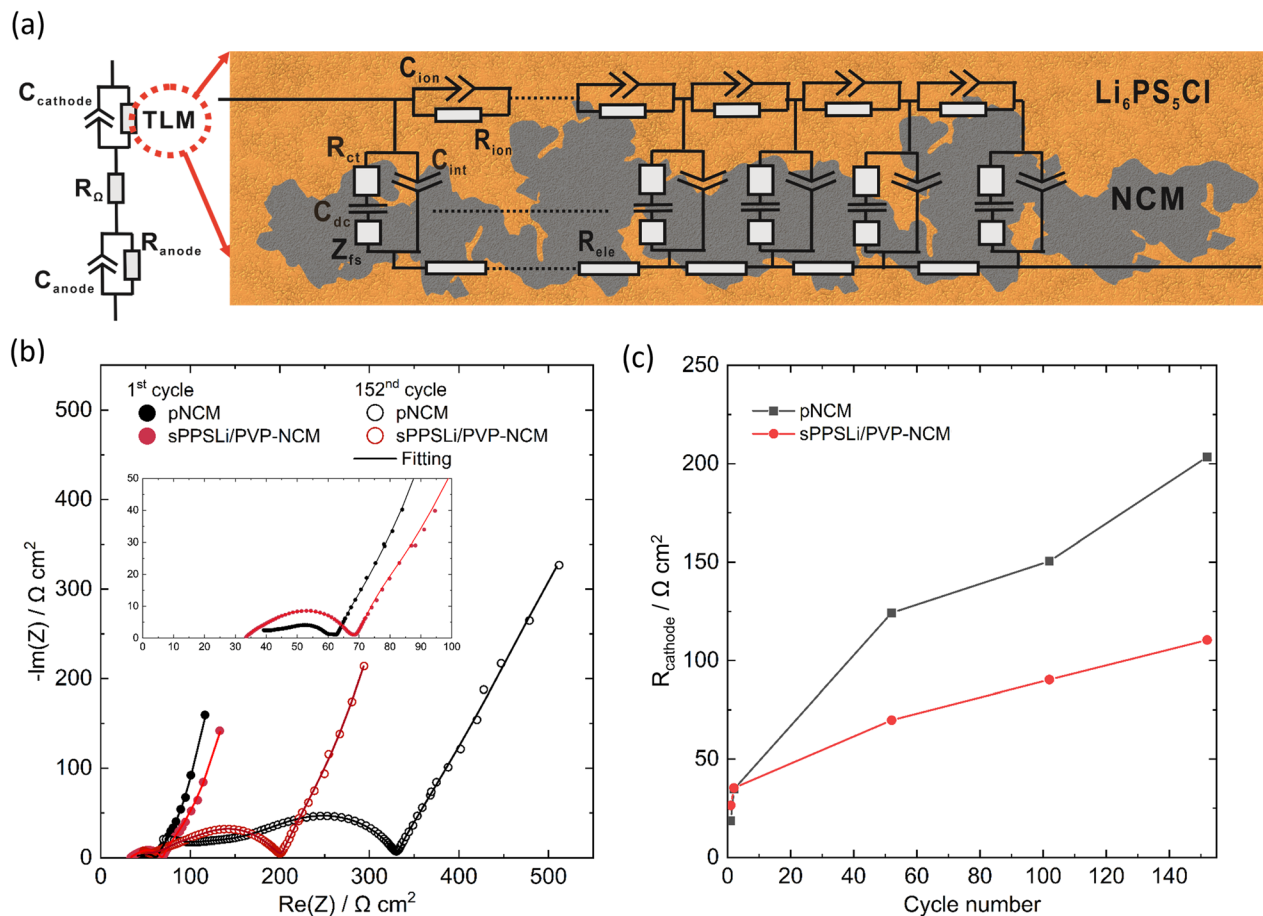This journal is © The Royal Society of Chemistry 2025

Fig. 5 (a) Equivalent circuit for impedance fitting in the form of the transition line model. R_{ct}, R_{ele}, and R_{ion} denote charge transfer, electronic, and ionic transport resistances in the cathode composite, respectively. Z_{fs} denotes the finite-space Warburg element of cylindrical particles. C_{dc} represents the differential capacitance of NCM, while C_{int} and C_{ion} signify interfacial and ionic transport capacitances. The full SEB model integrates the transition line model with R_Ω, R_{anode}, and C_{anode}. (b) Nyquist plots of ^{LiIn}SEB^{pNCM} and ^{LiIn}SEB$^{sPPSLi/PVP-NCM}$ at 25 °C during the 1st and 152nd cycles. (c) The $R_{cathode}$ values of different cycles of ^{LiIn}SEB^{pNCM} and ^{LiIn}SEB$^{sPPSLi/PVP-NCM}$ are compared.

3 nm coating might contribute around ∼3–9 Ω cm² of Li⁺ transport resistance.[26] These aspects necessitate further investigation of interface resistance (NCM/coating and coating/Li₆PS₅Cl) to elucidate the underlying mechanisms.

During cycling, $R_{cathode}$ for pNCM exhibits a more pronounced increase than that of sPPSLi/PVP-NCM: 151 Ω cm² for pNCM and 90 Ω cm² for sPPSLi/PVP-NCM after 102 cycles, and 203 Ω cm² for pNCM and 110 Ω cm² for sPPSLi/PVP-NCM after 152 cycles. This results in $R_{cathode}$ for pNCM being about 1.8 times that of the sPPSLi/PVP-NCM after 152 cycles (see Fig. 5b and c). The notable increase in $R_{cathode}$ for pNCM after cycling may be due to contact loss at the NCM/SE interface. This result is consistent with the lower m_{act} retention for pNCM compared to sPPSLi/PVP-NCM after cycling, as discussed above.

ToF-SIMS is performed to identify the decomposition products and to reveal the influence of the sPPSLi/PVP coating on the interfacial degradation due to electrochemical cycling. It allows the detection of interfacial decomposition products such as phosphates and sulfates in the composite cathode, which was comprehensively described by Walther *et al.*[30,72,73] Using this method, the surfaces of the composite cathodes with sPPSLi/PVP-NCM and pNCM were analyzed before cycling and after

152 cycles. Therefore, the current collector of cycled SEBs was removed to access the critical interfaces in the composite cathode. Since the sPPSLi/PVP coating in this work contains SO_2^- groups, the analysis of sulfate/sulfite fragments can lead to misinterpretations of ToF-SIMS data. Thus, only phosphates are considered in the following analysis. Since TOF-SIMS is a mass spectrometry technique that detects fragments generated by Bi^{3+} primary ions, PO_2^- and PO_3^- are sufficient to differentiate phosphorus oxide compounds, while PO^- does not directly represent stable phosphorus oxide compounds.[67,72] In this context, it should be noted that ToF-SIMS is a semi-quantitative method, as signal intensity depends not only on the concentration of the species but also on the chemical surrounding of the analyte (matrix effects).

In Fig. 6a, the mass spectra of PO_2^- and PO_3^- before cycling and after 152 cycles are exemplarily shown. The amount of PO_x^- fragments, in particular PO_2^- and PO_3^-, is lower for the coated than for the uncoated sample, which indicates that the coating reduces the formation of phosphates during cycling. Consequently, decomposition of the solid electrolyte is reduced by the protective function of the sPPSLi/PVP coating. Still, some decomposition products can be detected. This may be caused by
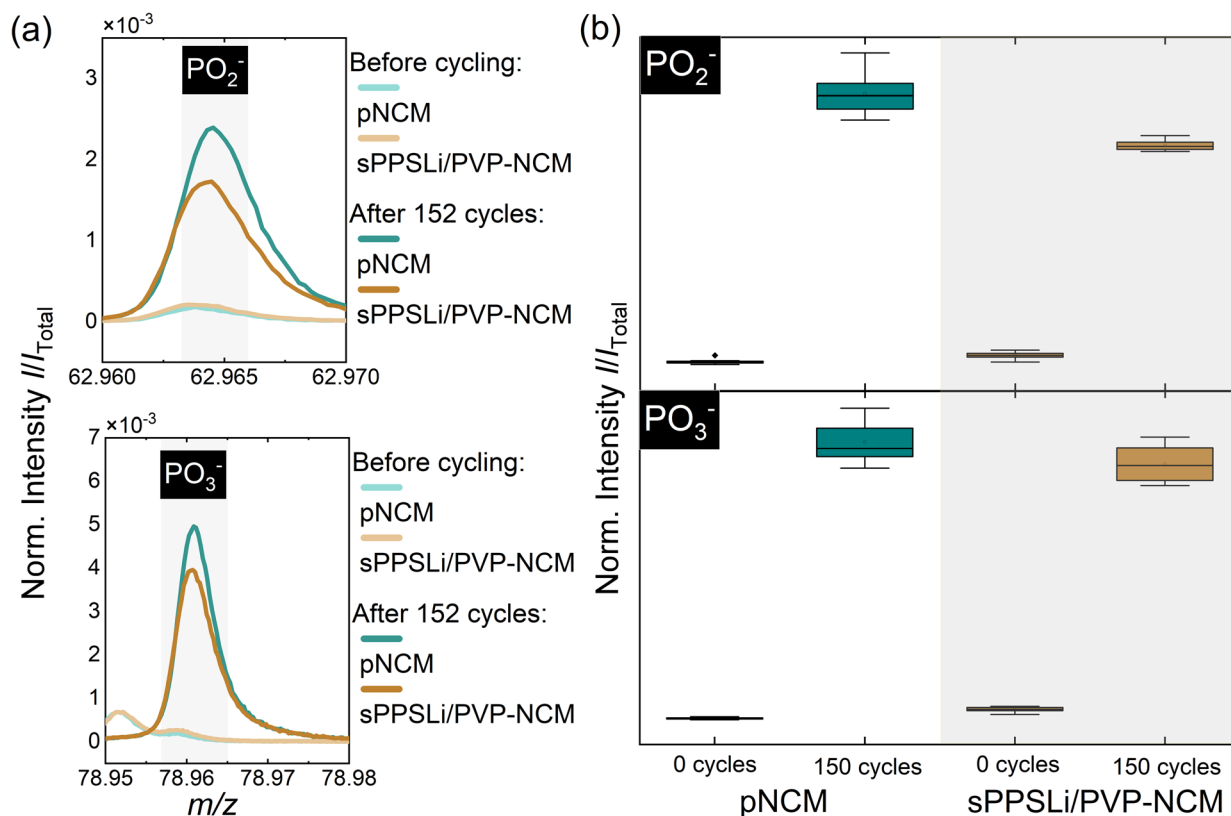
This journal is © The Royal Society of Chemistry 2025

J. Mater. Chem. A, 2025, **13**, 2600–2614 | **2607**

Fig. 6 (a) ToF-SIMS mass spectra for fragments that can be attributed to oxidative interfacial degradation products, such as PO_2^- and PO_3^- for pNCM and sPPSLi/PVP-NCM before cycling and after 152 cycles. (b) Corresponding boxplots of normalized intensities for degradation signals containing eight data points each.

partial detachment of the coating during preparation of the cathode composite, which was ground in an agate mortar. To ensure sufficient statistics and reliability of the data, eight mass spectra at different positions on the same sample were measured before and after cycling. The resulting data is summarized in box plots for semiquantitative comparison in Fig. 6b. The data confirms that the sPPSLi/PVP coating results in less decomposition products in the composite cathodes after electrochemical cycling. In summary, ToF-SIMS analysis of oxidative decomposition products indicates that using a sPPSLi/PVP coating enhances the interfacial stability at the NCM/SE interface, compared to pNCM. This evidence aligns with the results of electrochemical impedance spectroscopy.

2.6 Analysis of Li⁺ diffusion pathway length

The growth of the Li⁺ diffusion pathway length (L_{diff}) gives rise to capacity decay during battery cycling. Factors such as particle cracking within the NCM and the passivation layer obstructing Li⁺ and electron transport can extend L_{diff}. The value of L_{diff} within the cathode composite is determined by fitting the Warburg impedance. The fitting is obtained from the EIS results using the finite-space Warburg element of cylindrical particles (Z_{fs}), with the particle size distribution model (EIS-PSD) (Fig. 5a).[23,54] In addition, chronoamperometry also provides valuable insights into L_{diff}.[54]

The finite-space Warburg impedance is generally used to model the diffusion process across the entire volume of

a sample, accounting for the ion-blocking boundary at the current collector as well as the inner core of the NCM particles. When the frequency is sufficiently low to reach the ion-blocking border, a continuous transition is observed in the Nyquist plot, ranging from 45° and gradually approaching 90°.[74,75] As a result, to accurately determine the finite-space Warburg impedance through EIS, the lower frequency limit is set at 100 μHz. The finite-space Warburg element of cylindrical particles ($Z_{fs}^{cylindrical}$) delineates the intricate geometry of Li⁺ diffusion within the NCM. The thickness of the cylindrical particle can be taken as L_{diff}, acquired by fitting the EIS finite space diffusion tail using eqn (4) and (5) with the transition line model.

$$\tau_i = L_{diff}^2 / \tilde{D}_{Li} \tag{4}$$

and

$$Z_{fs}^{cylindrical} = \frac{1}{C_{diff}} \left(\sum_i \frac{\Delta\phi_i}{\tau_i} \frac{\sqrt{i\omega\tau_i}}{\coth\sqrt{i\omega\tau_i}} \right) \tag{5}$$

In eqn (4), τ_i is the characteristic time constant of Li⁺ diffusion. The diffusion coefficient of Li⁺ in NCM ($\tilde{D}_{Li}$) is assumed to be around 10^{-11} cm² s⁻¹ at 25 °C.[23,54] In eqn (5), the volume fraction of the particle contribution is denoted as $\Delta\phi_i$, indicating the amount of the NCM particle which has L_{diff} of τ_i to reach the finite condition. $C_{diff} = dq/dE$ equating to 392 mA h V⁻¹ g⁻¹ is the total differential capacity at 3.15 V (vs. In/LiIn) calculated

2608 | *J. Mater. Chem. A*, 2025, **13**, 2600–2614

This journal is © The Royal Society of Chemistry 2025

from cycling results of a $^{Li}LEB^{NCM}$ (see Fig. S11†). ω is the radial frequency. Fitting of the impedance data leads to L_{diff} and $\Delta\phi_i$, presented cumulatively in Fig. 7a.

At the initial cycle at 3.15 V (*vs.* In/LiIn), pNCM and sPPSLi/PVP-NCM show comparable L_{diff}, around 1.3 μm, matching the NCM particle radius. By the 152nd cycle, the L_{diff} for pNCM is twice as large as that for sPPSLi/PVP-NCM (5.2 μm for pNCM and 2.5 μm for sPPSLi/PVP-NCM). In conclusion, EIS-PSD fitting results show that a 1 wt% sPPSLi/PVP polymer coating layer mitigates the growth of L_{diff}. Fig. 7b shows that the chronoamperometry results confirm the conclusion of EIS-PSD.[23] The time it takes for the current to decrease below 2% is directly proportional to L_{diff}.[54,76] Initially, pNCM and sPPSLi/PVP-NCM exhibit an identical current reduction time, indicating that they possess the same L_{diff}. However, pNCM takes around 800 minutes at the 152nd cycle, whereas sPPSLi/PVP-NCM takes only about 400 minutes at the 152nd cycle. Overall, both EIS-PSD analysis and chronoamperometry results show that the L_{diff} for sPPSLi/PVP-NCM is about half that of pNCM after 152 cycles. This

result aligns with the higher capacity loss in pNCM than sPPSLi/PVP-NCM due to higher L_{diff}, as shown in Fig. 4c and d.

2.7 SEM cross-sections of NCM cathode before and after cycling

Using ion beam milling with SEM, we examine the morphology changes within cross-sections of composite cathodes of $^{LiIn}SEB^{pNCM}$ and $^{LiIn}SEB^{sPPSLi/PVP-NCM}$ after 152 cycles under 0.1C. The NCM particles appear as brighter areas in the SEM images, whereas Li_6PS_5Cl is represented by the darker regions. Before cycling, the coated NCM cathode composite shows no noticeable differences compared to the pristine one. The cracking that
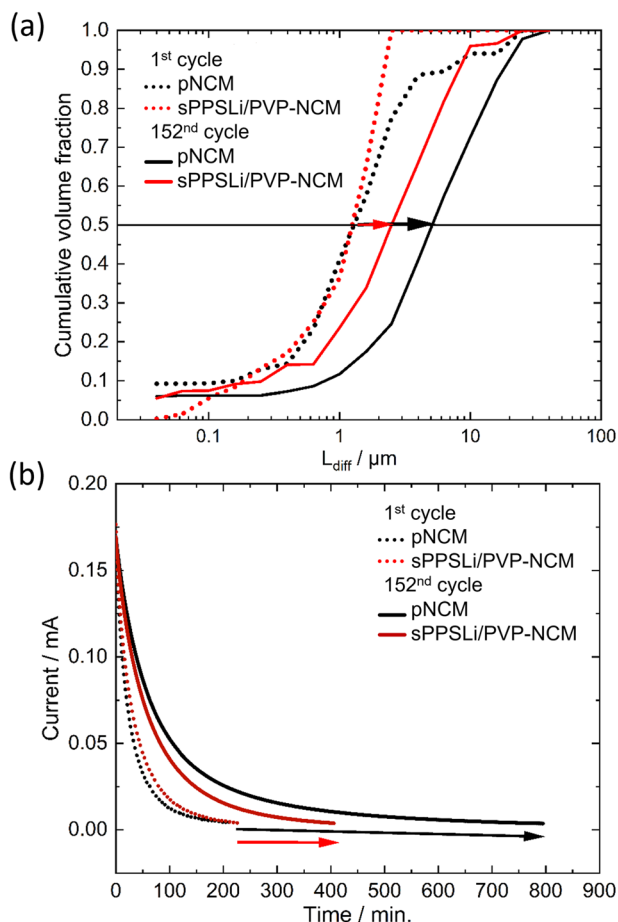
Fig. 7 (a) L_{diff} obtained using the EIS-PSD model for $^{LiIn}SEB^{pNCM}$ and $^{LiIn}SEB^{sPPSLi/PVP-NCM}$ in the 1st and 152nd cycles. The Warburg impedance is fitted through the EIS-PSD model to yield the cumulative volume fraction of particle size of different L_{diff}. (b) The chronoamperometry measurement shows the duration required for the current to drop below 2% of the initial charging current, which is proportional to L_{diff}.
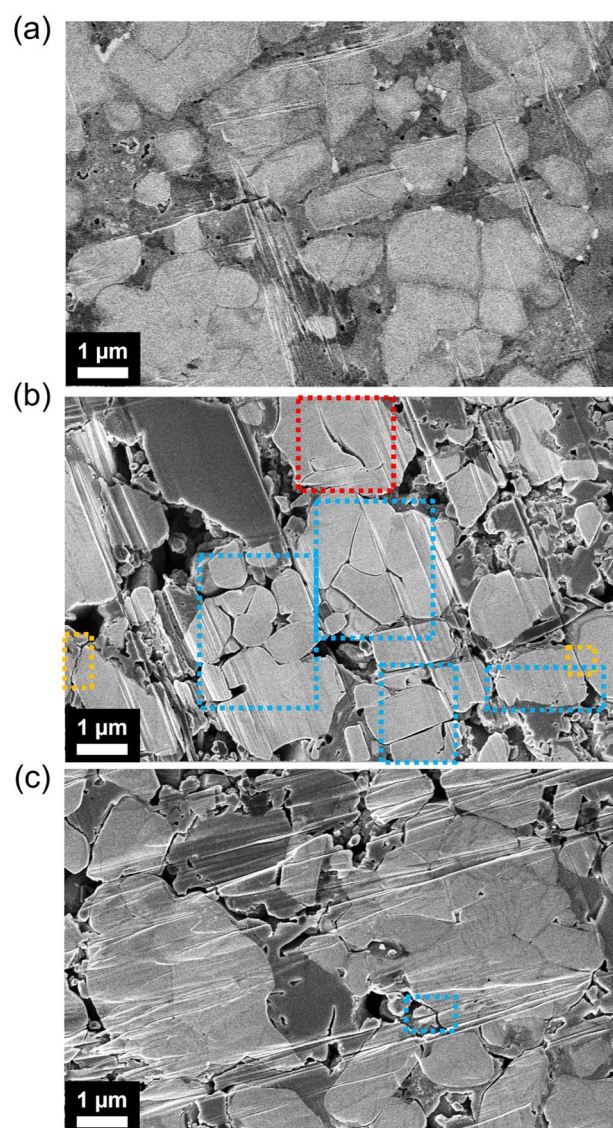
Fig. 8 SEM images of composite cathodes cross-sectioned by ion beam milling. (a) Li_6PS_5Cl/VGCF/pNCM cathode composite before cycling, (b) Li_6PS_5Cl/VGCF/pNCM cathode composite after 152 cycles at a rate of 0.1C, and (c) Li_6PS_5Cl/VGCF/sPPSLi/PVP-NCM cathode composite after 152 cycles at a rate of 0.1C. The red box indicates primary particle cracking, the orange box marks intergranular particle cracking, and the blue box highlights cracking that may be due to either of these causes.

This journal is © The Royal Society of Chemistry 2025

J. Mater. Chem. A, 2025, **13**, 2600–2614 | **2609**

separates whole particles is likely due to intergranular particle cracking. On the other hand, cracking occurring within a particle but not entirely separating the two particles is referred to as primary particle cracking. After 152 cycles, sPPSLi/PVP-NCM has fewer fractures within its particles than pNCM, as shown in Fig. 8. However, both SEBs show physical separation between NCM and Li_6PS_5Cl after cycling.

The reduced number of fractures may be due to less interfacial side reactions during cycling and less extraction of Li^+ from sPPSLi/PVP-NCM.[24] If the Li^+ extraction from NCM is relatively small, especially during the H2 + H3 phase transition, the particles are less likely to fracture.[77] However, the area under the differential capacity plots at around 3.48 V (*vs.* In/LiIn) of the first cycle is similar for pNCM and sPPSLi/PVP-NCM (Fig. 3). This indicates that both SEBs undergo comparable H2 + H3 phase transition processes. Therefore, we can rule out reduced Li^+ extraction from sPPSLi/PVP-NCM as the cause of the reduced cracking. On the other hand, a thin coating of only a few nanometers likely does not suppress the volumetric changes that occur in NCM during cycling. As a result, the cracking within sPPSLi/PVP-NCM particles may be mitigated by minimizing side reactions at the NCM/SE interface during cycling. Overall, sPPSLi/PVP-NCM has lower L_{diff} than pNCM due to less cracking within the particles.

3. Conclusion

To improve capacity retention of NCM in solid-state batteries, we present a sPPSLi/PVP polymer coating applied on NCM particles through spray drying. Nano-IR imaging, TEM images, and SIMS analysis show uniform coverage of NCM by a 1–3 nm thick sPPSLi/PVP layer. Electrochemical tests highlight enhanced cycling stability and rate performance of sPPSLi/PVP-NCM over the uncoated pNCM. The sPPSLi/PVP coating improves battery performance by stabilizing the NCM/Li_6PS_5Cl interface and shortening the Li^+ diffusion pathway compared to pNCM. In the rate capability test, sPPSLi/PVP-NCM consistently outperforms pNCM and other polymer-coated NCMs for all tested C-rates (0.1–1C). Results from the ToF-SIMS analysis of oxidative decomposition products and electrochemical impedance spectroscopy confirm the improvement of interfacial stability at the NCM/Li_6PS_5Cl interface during cycling. Moreover, the $^{LiIn}SEB^{sPPSLi/PVP-NCM}$ exhibits a shorter L_{diff} compared to the $^{LiIn}SEB^{pNCM}$ after cycling, as evidenced by EIS-PSD analysis and chronoamperometry. SEM images of composite cathode cross-sections show that a 1–3 nm thick sPPSLi/PVP coating can mitigate particle cracking, leading to enhanced solid-state battery performance. It is evident that polymer coatings can be used to improve cycling performance, which demonstrates the significance of applying polymer coatings in developing high-performance batteries.

4. Experimental methods

4.1 Reagents and materials

VGCF and DMF are purchased from Sigma-Aldrich. $LiNi_{0.9}Mn_{0.05}Co_{0.05}O_2$ is purchased from MSE Supplies, with a particle size between 2.0 μm and 6.0 μm and a Brunauer–Emmett–Teller (BET) specific surface area of approximately 0.90 ± 0.25 m^2 g^{-1}. Li_6PS_5Cl is purchased from NEI Corporation. Indium foil with a thickness of 100 μm is sourced from chemPUR GmbH and punched into a 9 mm diameter circular disc. Lithium foil with a thickness of 125 μm is purchased from Albemarle Rockwood Lithium GmbH and punched into a 6 mm diameter circular disc. PVBTATFSI[54] and sPPSLi[56] are synthesized following the respective literature procedures.[55,56] The molecular weight of the sPPSLi polymer is 102 kDa (weight average, determined by gel permeation chromatography) with a polydispersity index of 1.76. PVP (K30) with a molecular weight around 40 kDa is purchased from Sigma-Aldrich.

4.2 Polymer-coated NCM and VGCF

A mini-Spray Dryer B-290 from BUCHI is used to coat various polymers on NCM and VGCF, including PVBTATFSI, sPPSLi, PVP, and sPPSLi/PVP (1 : 1 ratio of weight). Firstly, 20 mg of polymer (1 wt% compared to NCM) is mixed with 2 g of NCM and 30 g of DMF as the NCM precursor suspension. For VGCF precursor suspension, 50 mg of polymer (10 wt% compared to VGCF) is mixed with 500 mg of VGCF and 30 g of DMF. This mixture is stirred vigorously for 1 hour before spray drying. However, the VGCF precursor is first sonicated by ultrasonic cleaner (VWR®) for 1 hour and then stirred vigorously for 1 hour before spray drying. The inlet temperature for spray drying is set to 200 °C, which is much higher than the DMF boiling point (153 °C). The suction of the vacuum pump is set to 37 m^3 h^{-1}. The feed rate of precursor solution is 4 mL min^{-1} if using DMF as the solvent. The N_2 flow is set to 40 L min^{-1}. The spray drying conditions are optimized to get the highest productivity around 75%. After spray drying, sPPSLi/PVP polymer coated VGCF, sPPSLi/PVP-NCM, PVP-NCM, and PVBTATFSI-NCM are dried in vacuum oven at 80 °C for 72 hours.

4.3 X-ray diffraction (XRD)

XRD is used to check the chemical stability between the sPPSLi/PVP polymer and Li_6PS_5Cl by using a Panalytical Empyrean XRD with Cu Kα radiation. Diffraction patterns are collected in a 2θ angular range from 10° to 85° with a step size of 0.026°, 0.04 rad. soller slits, and 1/2° anti-scatter slit. To check the chemical stability between the sPPSLi/PVP polymer with Li_6PS_5Cl, the sPPSLi/PVP polymer is mixed with Li_6PS_5Cl in a weight ratio of 1 : 1 (around 500 mg in total) by grinding in an agate mortar and then pressed into pellets (8 mm in diameter). After that, the pellets are heated and maintained at 80 °C for 24 hours, followed by a grinding process in the agate mortar to turn pellets into powder. Finally, the sPPSLi/PVP polymer powder after heating is characterized by XRD and compared with pristine Li_6PS_5Cl.

4.4 Fourier-transform infrared spectroscopy (FTIR)

FTIR spectra are recorded with a total number of 96 scans on an ATR-FTIR Thermo Fischer Scientific iD5 ATR spectrometer (550–4000 cm^{-1}). To check the chemical stability between sPPSLi/PVP with Li_6PS_5Cl, the sPPSLi/PVP polymer is mixed

2610 | *J. Mater. Chem. A*, 2025, **13**, 2600–2614

This journal is © The Royal Society of Chemistry 2025

with Li_6PS_5Cl in a weight ratio of 1 : 1 (around 500 mg in total) by grinding in an agate mortar and then pressed into pellets (8 mm in diameter). Subsequently, the pellets are heated and maintained at 80 °C for 24 hours. FTIR spectra are measured in pellet form before and after the heating process.

4.5   Scanning electron microscopy (SEM)

SEM (Merlin, Zeiss) at an acceleration voltage of 3 kV and acceleration current of 200 pA is adopted to characterize the morphology of NCM and particle cracking in the cathode composite after cycling. Back-scattered electron images and secondary electron images are recorded. For characterization of pNCM and sPPSLi/PVP-NCM, samples are measured in powder form, sticking tightly on the conductive copper tape. The particle cracking in the cathode composite after cycling is examined using SEM images taken following ion beam milling (Leica EM TIC 3X). Ion beam milling is conducted at 6 kV and 2 mA for 6 hours, at a temperature of −80 °C.

4.6   Transmission electron microscopy (TEM)

As the polymer is mainly made of the light element carbon, whereas NCM consists of heavier transition metals, the materials exhibit a different contrast in TEM bright field images. These images are recorded with a TVIPS TEMCam XF416FS camera on a JEOL JEM-3010 microscope at 300 kV acceleration voltage. For this purpose, powder of uncoated or coated NCM particles is sprinkled on a holey carbon copper TEM grid. Loose powder is removed by evacuating the TEM holder in a pumping stand before transferring it to the TEM to preserve the TEM vacuum.

4.7   Time-of-flight secondary ion mass spectrometry (ToF-SIMS)

Time-of-flight secondary ion mass spectrometry (ToF-SIMS) is carried out using a M6 Hybrid SIMS (IONTOF GmbH) equipped with a 30 kV Bi-cluster primary ion gun for analysis. During ToF-SIMS measurements, charged fragments are obtained through a collision cascade caused by the impact of the high-energy primary ion beam. All samples are prepared in a glovebox, attached to the sample holder using non-conductive adhesive tape and transferred to the SIMS instrument using the LEICA EM VCT500 shuttle (Leica Microsystems). In this work, sPPSLi and PVP polymers are first investigated in pure form and then compared with pristine and coated NCM. In addition, pristine (before cycling) and cycled (after cycling) composite cathodes are analyzed with uncoated and coated NCM. Therefore, the stainless-steel current collector was removed after cycling. All samples were prepared in the same way and under the same conditions. If not specified otherwise, the instrument was operated in the spectrometry mode using Bi_3^+ as primary ion species (0.19 pA) in the negative mode, which provides high mass resolution (full width at half maximum (FWHM) $m/\Delta m >$ 16 000 @ $m/z = 62.97$ (PO_2^-)). The analysis area is set to 75 × 75 μm^2, which is scanned with 64 × 64 pixels and a primary ion dose of 10^{12} ions cm^{-2} to keep the static limit. The spectra are calibrated on the following species: C^-, C_2^-, C_3^-, C_4^-, PO^-,

PO_2^- and PO_3^-. To ensure reliability of our data, 8 mass spectra were measured per sample. For imaging, Bi_3^+ as primary ion species in imaging mode was used (0.11 pA). The area for imaging is set to 20 × 20 μm^2, which is scanned with 256 × 256 pixels. The evaluation of the ToF-SIMS data was performed with the software SurfaceLab 7.3 (IONTOF GmbH).

4.8   Scanning force microscopy based infrared spectroscopy (nano-IR)

We perform nano-IR using the photo-induced force microscopy mode in the Visa Scope by Molecular Vista. We measure surface topography and photo-induced force microscopy amplitude simultaneously. For the topography measurement, we mechanically excite the cantilever at its second resonance frequency. The topography is recorded by an electronic feedback loop that kept the amplitude of the oscillation constant by varying the tip-sample distance. The photo-induced force microscopy amplitude is recorded at the first resonance frequency of the cantilever. This is achieved by modulating the incoming IR light at a frequency equal to the difference between the first and second eigenmodes. In this way, the modulated IR light generates a sideband of the excitation at the second resonant frequency, which is located at the first resonance frequency. Spectra of the photo-induced force microscopy amplitude are recorded by sweeping the wavenumber of the IR light. During the recording of the spectra, the incoming laser power is kept constant using a polariser. The spectral data was exported and then imported into OriginPro 2022 (version 9.9.0.225). Each individual spectrum is normalized based on its maximum photo-induced force microscopy amplitude. The data was then smoothed using the adjacent averaging filter with an averaging window of 10 pixels. Data visualization for the topography and nano-IR signal mapping was performed by Surface Works 3.0 by Molecular Vista and Inkscape 1.3.

4.9   Electrode composite and cell assembly

Cell tests are conducted using pellet-type cells inside an argon-filled glovebox (LabMaster, MBraun, Garching, Germany) with less than 0.1 ppm each of O_2 and H_2O. For most electrochemical analysis except cyclic voltammetry and ionic conductivity tests, asymmetric cells for rate capability and cycling performance are assembled as $InLi|Li_6PS_5Cl|Li_6PS_5Cl$, VGCF, and NCM. First, 80 mg of Li_6PS_5Cl is pressed into a 10 mm diameter pellet inside a cylindrical PEEK insulator. The cathode composite is formed by mixing the weight ratio of 69.3% NCM (either pristine or coated), 29.7% Li_6PS_5Cl, and 1% VGCF. This mixture is ground in an agate mortar for about 20 minutes. 12 mg of this cathode mixture is then pressed onto one side of the electrolyte, resulting in an area mass loading of 10.6 mg cm^{-2}. On the opposite side, indium (100 μm thick, 9 mm diameter) and lithium foils (125 μm thick, 6 mm diameter) serve as the anode. Post-assembly, the cell is compressed under 30 kN for 3 minutes using automatic press Atlas Autotouch automatic press, yielding a 400 μm solid electrolyte alongside a 30 μm composite cathode. During the analysis, the assembled cell is placed in an external aluminum frame exerting approximately 50 MPa of

This journal is © The Royal Society of Chemistry 2025

J. Mater. Chem. A, 2025, **13**, 2600–2614 | **2611**

stack pressure. A cross-sectional representation of this assembly is shown in Fig. S9a.†

For cyclic voltammetry, the cell setup is $LiIn|Li_6PS_5Cl|Li_6$-$PS_5Cl/VGCF$ in which the VGCF is either polymer-coated or pristine VGCF. To make a 100 mg cathode composite, 9.1 mg of VGCF is combined with 90.9 mg Li_6PS_5Cl and ground for 20 minutes. 80 mg of Li_6PS_5Cl is then pressed into a 10 mm diameter pellet inside the PEEK insulator as a separator. This is followed by pressing 30 mg of the Li_6PS_5Cl-VGCF-composite onto one side of the electrolyte. Like the previous assembly, indium and lithium foils are pressed on the opposite side of the anode. The cell stack is compressed under 30 kN for 3 minutes using automatic press Atlas Autotouch automatic press. During the analysis, the cell is positioned inside an external aluminum frame exerting around 50 MPa.

For the ionic conductivity measurement of the polymer, the cell setup is assembled as follows. Firstly, 0.16 g of dried polymer powder is compressed into a 10 mm diameter pellet in the PEEK at 30 kN for 3 minutes using automatic press Atlas Autotouch automatic press. To make sure that there is no moisture influencing the ionic conductivity, the pellet is further dried under vacuum ($\sim10^{-2}$ mbar) and 120 °C for 72 hours. Subsequently, both sides are coated with platinum using the sputtering method (Leica Sputter Coater ACE600). Finally, stainless steel stamps are attached on both sides to complete the cell assembly.

4.10 Liquid electrolyte batteries (LEBs)

To create an OCV vs. capacity reference curve without the influence of contact loss between CAM and SE, a $^{Li}LEB^{NCM}$ is prepared. The cathode slurry is prepared by dispersing NCM, PVDF binder (Solef 5130, Solvay) and super-P carbon additives (Sigma-Aldrich) in a weight ratio of $94:3:3$ in NMP (Sigma-Aldrich). Then the cathode sheet is prepared by tape casting procedure using the cathode slurry (solid content 56% and doctor blade thickness of 60 μm). For cell assembly, a cathode with 12 mm diameter is punched from the dried sheet (120 °C for 12 h in vacuum) and pressed at 200 MPa. The electrolyte is 1 M $LiPF_6$ in EC : DEC (1 : 1 vol%) with a glass fiber separator and a Celgard separator (in contact with the cathode side). A 14 mm diameter lithium metal disc is used as the anode. CR2032 coin cell casings with aluminum coating on the cathode cases are used to avoid parasitic currents that appear especially in the first cycles. First two formation cycles to 4.17 V (vs. Li^+/Li) includes chronoamperometry at 3 V for 36 hours to ensure stable SEI formation. Then 0.1C pulses for 10 minutes with 2 h subsequent relaxation are applied 80 times with an upper cutoff voltage of 4.3 V (vs. Li^+/Li). This is repeated for the discharge. After this pulse-relaxation-procedure similar to GITT experiments, a final checkup cycle similar to the second formation cycle is applied to ensure that no drastic changes to the cell occurred during the experiment.

4.11 Electrochemical analysis

For the cycling stability test, $^{LiIn}SEB^{NCM}$ are charged and discharged under 0.1C (calculated based on the practical capacity of NCM, which is around 200 mA h g^{-1} and 2.1 mA h cm^{-2}) within a voltage window ranging from 2.0 V to 3.7 V (vs. In/LiIn)

at a constant temperature of 25 °C in a VMP-300 (BioLogic) electrochemical workstation to assess chronoamperometry and EIS. Batteries are first charged under 0.1C to a voltage of 3.15 V (vs. In/LiIn). Chronoamperometry is then performed continuously at this voltage until the observed current diminishes below 2% of the charging current. Subsequently, EIS measurements between 1 MHz and 100 μHz are carried out immediately after the chronoamperometry. EIS sinusoidal amplitudes are set at 10 mV (from 1 MHz to 10 mHz), 5 mV (from 10 mHz to 1 mHz), and finally, 3 mV (from 1 mHz to 100 μHz). Amplitudes are adjusted per frequency to approximate a linear current response and reduce errors. Smaller AC amplitudes enhance linearity. After that, the batteries are continuously charged and discharged at a rate of 0.1C. The MACCOR electrochemical workstation is used for continuous cycling stability testing with a constant current of 0.1C. The whole testing process is schematically shown in Fig. S9b.† The impedance fitting model is depicted in Fig. 5a, where the low-frequency segment is fitted with the finite-space Warburg impedance (Z_{fs}). For rate capability tests, SEBs are charged and discharged under C-rates of 0.1C, 0.25C, 0.5C, 1C. within a voltage window ranging from 2.0 V to 3.7 V (vs. In/LiIn) at a constant temperature of 25 °C in MACCOR electrochemical workstation.

Cyclic voltammetry experiments are conducted by a VMP-300 Biologic potentiostat at 25 °C to determine the electrochemical stability. The measurement protocol involves a two-electrode setup, with the LiIn anode as the reference and counter electrode. The initial voltage sweeps from the OCV to 4 V relative to the reference electrode at a 1 mV s^{-1} scan rate for the oxidative phase. Subsequently, this sweep direction is inverted until it reaches 0 V before returning to the original potential.

Additionally, the ionic conductivity of sPPSLi/PVP is measured by EIS using VMP-300 Biologic potentiostat with the climate chamber (Weiss Technik) controlling the temperature from 10 °C to 80 °C. EIS sinusoidal amplitude is set at 100 mV from 1 MHz to 100 mHz to enhance the AC current response, compensating for the low ionic conductivity of the polymer film.

Data availability

Supporting data for this article are provided in the ESI.† Additional raw data can be obtained from the corresponding authors upon request.

Author contributions

B. X. S. was responsible for the electrochemical analyses, and general characterization of materials. Y. Y. conducted the TOF-SIMS analysis, while T. D. performed the TEM experiments. F. W. and R. B. conducted the nano-IR analysis. K. V., A. H., and F. H. R. contributed to the analysis and interpretation of the experimental data. A. M. and G. T. provided the anionic polymer. The research concept was conceived by B. X. S. and F. H. R., who also prepared the manuscript. All authors contributed to the manuscript and the analysis of experimental results.

2612 | J. Mater. Chem. A, 2025, 13, 2600–2614

This journal is © The Royal Society of Chemistry 2025

Conflicts of interest

The authors declare no conflict of interest.

Acknowledgements

References

1 S. Sen and F. H. Richter, *Adv. Sci.*, 2023, **10**, 2303985.

2 J. Schnell, T. Günther, T. Knoche, C. Vieider, L. Köhler, A. Just, M. Keller, S. Passerini and G. Reinhart, *J. Power Sources*, 2018, **382**, 160–175.

3 D. H. S. Tan, Y. S. Meng and J. Jang, *Joule*, 2022, **6**, 1755–1769.

4 X. Yu, R. Chen, L. Gan, H. Li and L. Chen, *Engineering*, 2023, **21**, 9–14.

5 S. Sen, E. Trevisanello, E. Niemöller, B.-X. Shi, F. J. Simon and F. H. Richter, *J. Mater. Chem. A*, 2021, **9**, 18701–18732.

6 Q. Zhang, D. Cao, Y. Ma, A. Natan, P. Aurora and H. Zhu, *Adv. Mater.*, 2019, **31**, 1901131.

7 Y. Guo, S. Wu, Y.-B. He, F. Kang, L. Chen, H. Li and Q.-H. Yang, *eScience*, 2022, **2**, 138–163.

8 A. Banerjee, X. Wang, C. Fang, E. A. Wu and Y. S. Meng, *Chem. Rev.*, 2020, **120**, 6878–6933.

9 Y. Yusim, E. Trevisanello, R. Ruess, F. H. Richter, A. Mayer, D. Bresser, S. Passerini, J. Janek and A. Henss, *Angew. Chem., Int. Ed.*, 2023, **62**, e202218316.

10 R. Chen, Q. Li, X. Yu, L. Chen and H. Li, *Chem. Rev.*, 2020, **120**, 6820–6877.

11 S. Dühnen, J. Betz, M. Kolek, R. Schmuch, M. Winter and T. Placke, *Small Methods*, 2020, **4**, 2000039.

12 Y. Wang, Z. Wang, D. Wu, Q. Niu, P. Lu, T. Ma, Y. Su, L. Chen, H. Li and F. Wu, *eScience*, 2022, **2**, 537–545.

13 T. Demuth, T. Fuchs, F. Walther, A. Pokle, S. Ahmed, M. Malaki, A. Beyer, J. Janek and K. Volz, *Matter*, 2023, **6**, 2324–2339.

14 C. Yu, F. Zhao, J. Luo, L. Zhang and X. Sun, *Nano Energy*, 2021, **83**, 105858.

15 S.-K. Jung, H. Gwon, S.-S. Lee, H. Kim, J. C. Lee, J. G. Chung, S. Y. Park, Y. Aihara and D. Im, *J. Mater. Chem. A*, 2019, **7**, 22967–22976.

16 G. F. Dewald, S. Ohno, M. A. Kraft, R. Koerver, P. Till, N. M. Vargas-Barbosa, J. Janek and W. G. Zeier, *Chem. Mater.*, 2019, **31**, 8328–8337.

17 D. H. S. Tan, E. A. Wu, H. Nguyen, Z. Chen, M. A. T. Marple, J.-M. Doux, X. Wang, H. Yang, A. Banerjee and Y. S. Meng, *ACS Energy Lett.*, 2019, **4**, 2418–2427.

18 Y. Zhu, X. He and Y. Mo, *ACS Appl. Mater. Interfaces*, 2015, **7**, 23685–23693.

19 S. Wang, M. Tang, Q. Zhang, B. Li, S. Ohno, F. Walther, R. Pan, X. Xu, C. Xin, W. Zhang, L. Li, Y. Shen, F. H. Richter, J. Janek and C.-W. Nan, *Adv. Energy Mater.*, 2021, **11**, 2101370.

20 J. Auvergniot, A. Cassel, J.-B. Ledeuil, V. Viallet, V. Seznec and R. Dedryvère, *Chem. Mater.*, 2017, **29**, 3883–3890.

21 T. Bartsch, F. Strauss, T. Hatsukade, A. Schiele, A. Y. Kim, P. Hartmann, J. Janek and T. Brezesinski, *ACS Energy Lett.*, 2018, **3**, 2539–2543.

22 T.-T. Zuo, R. Rueß, R. Pan, F. Walther, M. Rohnke, S. Hori, R. Kanno, D. Schröder and J. Janek, *Nat. Commun.*, 2021, **12**, 6669.

23 G. Conforto, R. Ruess, D. Schröder, E. Trevisanello, R. Fantin, F. H. Richter and J. Janek, *J. Electrochem. Soc.*, 2021, **168**, 070546.

24 H. Zhang, H. Liu, L. F. J. Piper, M. S. Whittingham and G. Zhou, *Chem. Rev.*, 2022, **122**, 5641–5681.

25 T. Nakamura, K. Amezawa, J. Kulisch, W. G. Zeier and J. Janek, *ACS Appl. Mater. Interfaces*, 2019, **11**, 19968–19976.

26 S. P. Culver, R. Koerver, W. G. Zeier and J. Janek, *Adv. Energy Mater.*, 2019, **9**, 1900626.

27 J. Hertle, F. Walther, T. Lombardo, C. Kern, B. Pavlovic, B. Mogwitz, X. Wu, H. Schneider, M. Rohnke and J. Janek, *ACS Appl. Mater. Interfaces*, 2024, **16**, 9400–9413.

28 A. Y. Kim, F. Strauss, T. Bartsch, J. H. Teo, T. Hatsukade, A. Mazilkin, J. Janek, P. Hartmann and T. Brezesinski, *Chem. Mater.*, 2019, **31**, 9664–9672.

29 Y.-J. Kim, R. Rajagopal, S. Kang and K.-S. Ryu, *Chem. Eng. J.*, 2020, **386**, 123975.

30 F. Walther, F. Strauss, X. Wu, B. Mogwitz, J. Hertle, J. Sann, M. Rohnke, T. Brezesinski and J. Janek, *Chem. Mater.*, 2021, **33**, 2110–2125.

31 D. Kitsche, F. Strauss, Y. Tang, N. Bartnick, A.-Y. Kim, Y. Ma, C. Kübel, J. Janek and T. Brezesinski, *Batteries Supercaps*, 2022, **5**, e202100397.

32 R. S. Negi, Y. Yusim, R. Pan, S. Ahmed, K. Volz, R. Takata, F. Schmidt, A. Henss and M. T. Elm, *Adv. Mater. Interfaces*, 2022, **9**, 2101428.

33 F. Strauss, J. H. Teo, J. Maibach, A. Y. Kim, A. Mazilkin, J. Janek and T. Brezesinski, *ACS Appl. Mater. Interfaces*, 2020, **12**, 57146–57154.

34 R. S. Negi, P. Minnmann, R. Pan, S. Ahmed, M. J. Herzog, K. Volz, R. Takata, F. Schmidt, J. Janek and M. T. Elm, *Chem. Mater.*, 2021, **33**, 6713–6723.

35 S. H. Jung, K. Oh, Y. J. Nam, D. Y. Oh, P. Brüner, K. Kang and Y. S. Jung, *Chem. Mater.*, 2018, **30**, 8190–8200.

36 E. A. Wu, C. Jo, D. H. S. Tan, M. Zhang, J.-M. Doux, Y.-T. Chen, G. Deysher and Y. S. Meng, *J. Electrochem. Soc.*, 2020, **167**, 130516.

37 Y.-Q. Zhang, Y. Tian, Y. Xiao, L. J. Miara, Y. Aihara, T. Tsujimura, T. Shi, M. C. Scott and G. Ceder, *Adv. Energy Mater.*, 2020, **10**, 1903778.

This journal is © The Royal Society of Chemistry 2025

J. Mater. Chem. A, 2025, **13**, 2600–2614 | **2613**

38 J. S. Kim, S. Jung, H. Kwak, Y. Han, S. Kim, J. Lim, Y. M. Lee and Y. S. Jung, *Energy Storage Mater.*, 2023, **55**, 193–204.

39 A. Sakuda, A. Hayashi and M. Tatsumisago, *Curr. Opin. Electrochem.*, 2017, **6**, 108–114.

40 J. Chang, K. B. Toga, J. D. Paulsen, N. Menon and T. P. Russell, *Macromolecules*, 2018, **51**, 6764–6770.

41 J. Y. Chung, A. J. Nolte and C. M. Stafford, *Adv. Mater.*, 2011, **23**, 349–368.

42 S. Deng, Y. Sun, X. Li, Z. Ren, J. Liang, K. Doyle-Davis, J. Liang, W. Li, M. Norouzi Banis, Q. Sun, R. Li, Y. Hu, H. Huang, L. Zhang, S. Lu, J. Luo and X. Sun, *ACS Energy Lett.*, 2020, **5**, 1243–1251.

43 Q. Gan, N. Qin, Y. Zhu, Z. Huang, F. Zhang, S. Gu, J. Xie, K. Zhang, L. Lu and Z. Lu, *ACS Appl. Mater. Interfaces*, 2019, **11**, 12594–12604.

44 G.-L. Xu, Q. Liu, K. K. S. Lau, Y. Liu, X. Liu, H. Gao, X. Zhou, M. Zhuang, Y. Ren, J. Li, M. Shao, M. Ouyang, F. Pan, Z. Chen, K. Amine and G. Chen, *Nat. Energy*, 2019, **4**, 484–494.

45 S. H. Ju, I.-S. Kang, Y.-S. Lee, W.-K. Shin, S. Kim, K. Shin and D.-W. Kim, *ACS Appl. Mater. Interfaces*, 2014, **6**, 2546–2552.

46 Y.-S. Lee, W.-K. Shin, A. G. Kannan, S. M. Koo and D.-W. Kim, *ACS Appl. Mater. Interfaces*, 2015, **7**, 13944–13951.

47 Y. Huang, J. Xia, G. Hu, Y. Cao, Z. Peng, J. Fan, Y. Tao, T. Li, Z. Zhang, Z. Xue and K. Du, *Electrochim. Acta*, 2020, **332**, 135505.

48 Y. Cao, X. Qi, K. Hu, Y. Wang, Z. Gan, Y. Li, G. Hu, Z. Peng and K. Du, *ACS Appl. Mater. Interfaces*, 2018, **10**, 18270–18280.

49 E.-H. Lee, J.-H. Park, J.-H. Cho, S.-J. Cho, D. W. Kim, H. Dan, Y. Kang and S.-Y. Lee, *J. Power Sources*, 2013, **244**, 389–394.

50 H. Wang, J. Lin, X. Zhang, L. Wang, J. Yang, E. Fan, F. Wu, R. Chen and L. Li, *ACS Appl. Energy Mater.*, 2021, **4**, 6205–6213.

51 A. Yiğitalp, A. Taşdemir, S. Alkan Gürsel and A. Yürüm, *Energy Storage*, 2020, **2**, e154.

52 D. Becker, M. Börner, A. Friesen, S. Klein, U. Rodehorst, M. Diehl, M. Winter, T. Placke and R. Schmuch, *J. Electrochem. Soc.*, 2020, **167**, 060524.

53 B. Li, G. Li, D. Zhang, J. Fan, D. Chen, Y. Ge, F. Lin, C. Zheng and L. Li, *ChemistrySelect*, 2019, **4**, 6354–6360.

54 B.-X. Shi, Y. Yusim, S. Sen, T. Demuth, R. Ruess, K. Volz, A. Henss and F. H. Richter, *Adv. Energy Mater.*, 2023, **13**, 2300310.

55 C. C. de Araujo, K. D. Kreuer, M. Schuster, G. Portale, H. Mendil-Jakani, G. Gebel and J. Maier, *Phys. Chem. Chem. Phys.*, 2009, **11**, 3305–3312.

56 M. Schuster, K.-D. Kreuer, H. T. Andersen and J. Maier, *Macromolecules*, 2007, **40**, 598–607.

57 Y. Zhou, Z. Hu, Y. Huang, Y. Wu and Z. Hong, *J. Alloys Compd.*, 2021, **888**, 161584.

58 M. H. Pyun and Y. J. Park, *Nanoscale Res. Lett.*, 2016, **11**, 272.

59 C. Lau and Y. Mi, *Polymer*, 2002, **43**, 823–829.

60 A. A. Sifat, J. Jahng and E. O. Potma, *Chem. Soc. Rev.*, 2022, **51**, 4208–4222.

61 R. A. Murdick, W. Morrison, D. Nowak, T. R. Albrecht, J. Jahng and S. Park, *Jpn. J. Appl. Phys.*, 2017, **56**, 8S1.

62 C. Sprau, J. Kattenbusch, Y. Li, E. Müller, D. Gerthsen, R. Berger, J. J. Michels and A. Colsmann, *Sol. RRL*, 2021, **5**, 2100238.

63 T. Sui, B. Song, J. Dluhos, L. Lu and A. M. Korsunsky, *Nano Energy*, 2015, **17**, 254–260.

64 C. Hong, Q. Leng, J. Zhu, S. Zheng, H. He, Y. Li, R. Liu, J. Wan and Y. Yang, *J. Mater. Chem. A*, 2020, **8**, 8540–8547.

65 R. Koerver, I. Aygün, T. Leichtweiß, C. Dietrich, W. Zhang, J. O. Binder, P. Hartmann, W. G. Zeier and J. Janek, *Chem. Mater.*, 2017, **29**, 5574–5582.

66 S. Randau, F. Walther, A. Neumann, Y. Schneider, R. S. Negi, B. Mogwitz, J. Sann, K. Becker-Steinberger, T. Danner, S. Hein, A. Latz, F. H. Richter and J. Janek, *Chem. Mater.*, 2021, **33**, 1380–1393.

67 T.-T. Zuo, F. Walther, J. H. Teo, R. Rueß, Y. Wang, M. Rohnke, D. Schröder, L. F. Nazar and J. Janek, *Angew. Chem., Int. Ed.*, 2023, **62**, e202213228.

68 E. Trevisanello, R. Ruess, G. Conforto, F. H. Richter and J. Janek, *Adv. Energy Mater.*, 2021, **11**, 2003400.

69 W. Waag, S. Käbitz and D. U. Sauer, *Appl. Energy*, 2013, **102**, 885–897.

70 R. Ruess, S. Schweidler, H. Hemmelmann, G. Conforto, A. Bielefeld, D. A. Weber, J. Sann, M. T. Elm and J. Janek, *J. Electrochem. Soc.*, 2020, **167**, 100532.

71 J. Moškon and M. Gaberšček, *J. Power Sources Adv.*, 2021, **7**, 100047.

72 F. Walther, S. Randau, Y. Schneider, J. Sann, M. Rohnke, F. H. Richter, W. G. Zeier and J. Janek, *Chem. Mater.*, 2020, **32**, 6123–6136.

73 F. Walther, R. Koerver, T. Fuchs, S. Ohno, J. Sann, M. Rohnke, W. G. Zeier and J. Janek, *Chem. Mater.*, 2019, **31**, 3745–3755.

74 J. Song and M. Z. Bazant, *J. Electrochem. Soc.*, 2013, **160**, A15.

75 J. Song and M. Z. Bazant, *Electrochim. Acta*, 2014, **131**, 214–227.

76 M. D. Levi and D. Aurbach, *Charact. Mater.*, 2012, **3**, 913–932.

77 H. Li, A. Liu, N. Zhang, Y. Wang, S. Yin, H. Wu and J. R. Dahn, *Chem. Mater.*, 2019, **31**, 7574–7583.

2614 | *J. Mater. Chem. A*, 2025, **13**, 2600–2614

This journal is © The Royal Society of Chemistry 2025